International Journal of Heat and Fluid Flow 114 (2025) 109815

Contents lists available at ScienceDirect

International Journal of Heat and Fluid Flow

journal homepage: www.elsevier.com/locate/ijhff

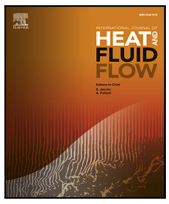

Investigation of turbulent/non-turbulent interfaces in high Reynolds number adverse pressure gradient boundary layers

Luka Lindić *, Wagih Abu Rowin, Rahul Deshpande, Ivan Marusic

Department of Mechanical Engineering, University of Melbourne, Parkville VIC 3010, Melbourne, 3055, Victoria, Australia

ARTICLE INFO

Keywords:
Turbulent boundary layers
Adverse pressure gradient
High Reynolds numbers
Turbulent/non-turbulent interface
Vorticity
Local kinetic energy

ABSTRACT

This study utilises high-magnification two-dimensional Particle Image Velocimetry (2D-PIV) to investigate adverse pressure gradient (APG) turbulent boundary layers at high friction Reynolds numbers, which evolve from a canonical zero pressure gradient (ZPG) upstream condition. The primary focus is on comparing the turbulent/non-turbulent interface (TNTI) for ZPG and APG at high Reynolds number. Local kinetic energy (LKE) and spanwise vorticity methods are considered for TNTI detection, with Joint Probability Density Functions (JPDFs) for LKE/vorticity and wall-normal distance used to determine the respective thresholds and estimate corresponding TNTI heights. A sensitivity analysis of the mean TNTI height with respect to the selected threshold for distinguishing turbulent and non-turbulent regions is conducted for both methods, with the LKE method demonstrating a lower sensitivity to the threshold compared to vorticity. The results confirm the inadequacy of using in-plane vorticity for the current experimental data while also highlighting the limitations of the LKE method. Overall, the present findings based on relatively small thresholds support a decrease in normalised TNTI height with increasing adverse pressure gradients at high Reynolds number, demonstrating consistency with previous low Reynolds number results. Conditional averaging analysis is conducted for the instantaneous streamwise and wall-normal velocities based on TNTI height, confirming that the APG outer wake region is distinctly different to the ZPG case. For the APG flow, the spread in the conditional averaged velocity curves is larger than in the ZPG case, with the start of the deviation from the mean velocity profile occurring closer to the normalised position from the wall.

1. Introduction

The seminal work by Corrsin and Kistler (1955) laid the foundation for a comprehensive investigation of the turbulent/non-turbulent interface (TNTI) in wall-bounded flows under zero-pressure-gradient (ZPG) conditions. This foundational work has been expanded upon by numerous subsequent studies, including those by Klebanoff (1955), Chauhan et al. (2014), and da Silva et al. (2014), amongst many others (Wang and Marusic, 2024). The TNTI is characterised by its complex, fractal-like geometry (Sreenivasan et al., 1989), which spans all scales, from the smallest to the largest turbulent eddies, making its accurate capture a challenging task.

Towards addressing these challenges, Reuther and Kähler (2018) compared TNTI detection using different seeding methods and three distinct techniques—turbulent kinetic energy, homogeneity of the non-turbulent flow region, and particle image density—highlighting the sensitivity and robustness of these approaches for TNTI measurement. The TNTI also imparts an intermittent character to measurements, evident in hot-wire signals and velocity field data obtained through particle image velocimetry (PIV) or direct numerical simulation (DNS).

In recent years, the increasing height of wind turbines, both as standalone structures and integrated into tall buildings, has raised the likelihood of encountering TNTI-like behaviour in atmospheric turbulent boundary layer flows. In particular, understanding and determining interface heights can potentially aid in designing wind turbines that operate within the atmospheric surface layer/boundary layer interface, optimising their performance and resilience under such conditions (Neuhaus et al., 2023; Škvorc and Kozmar, 2021).

The vast majority of prior studies on turbulent boundary layer TNTIs have focused on ZPG conditions, either experimentally or numerically. In contrast, the study by Yang et al. (2020) stands out as the only research to date that examines APG boundary layers. Yang et al. (2020) investigated how an APG affects a turbulent boundary layer (TBL) by analysing the geometry and entrainment at the TNTI. Using DNS data, they compared an APG TBL ($\beta = 1.45$) and a ZPG TBL ($\beta = 0$), identifying interfaces where the turbulent region meets the irrotational region. Their analysis showed that the APG significantly enhances the formation of vortical structures in the outer region due to increased

* Corresponding author.
E-mail address: luka.lindic.ll@gmail.com (L. Lindić).

https://doi.org/10.1016/j.ijheatfluidflow.2025.109815
Received 1 November 2024; Received in revised form 9 February 2025; Accepted 10 March 2025
Available online 26 March 2025

Table 1
Overview of various methods used to estimate average TNTI heights and statistics for ZPG and APG TBLs.

ZPG	$Re_\tau = \delta_{99}\overline{U}_\tau/\nu$	$\overline{Z_i}/\delta_{99}$	σ_i/δ_{99}	σ_i/Z_i	Method
Klebanoff (1955)	–	0.78	0.024	–	Vorticity
Kovasznay et al. (1970)	1240	0.78	0.14	0.18	Der. of streamwise velocity
Hedley and Keffer (1974)	5100	0.75	0.24	0.32	Der. of streamwise velocity
Chen and Blackwelder (1978)	1190	0.82	0.13	0.16	Der. of streamwise velocity
Murlis et al. (1982)	1450	0.8	0.024	–	Vorticity
Jiménez et al. (2010)	692	0.92	0.018	–	Vorticity
Semin et al. (2011)	600	0.77	0.09	0.15	Vorticity
Chauhan et al. (2014)	14 500	0.9	0.11	0.167	LKE
Eisma et al. (2015)	2053	0.9	–	–	Vorticity
Watanabe et al. (2018)	–	0.9	–	–	Vorticity, LKE
Yang et al. (2020)	825	0.95	–	–	Vorticity
Present study	7500	0.9154	0.1127	0.1231	LKE
Present study	7500	0.9345	0.1213	0.1298	Vorticity
APG					
Yang et al. (2020), $\beta = 1.45$	725	0.85	–	–	Vorticity
Present study	7100	0.8430	0.0965	0.1145	LKE
Present study	7100	0.8786	0.1062	0.1208	Vorticity

energy, leading to a larger projection area of the genus in the APG TBL compared to the ZPG TBL. This increased complexity and energy at the TNTI enhances the entrainment phenomenon, leading to notable changes in turbulence statistics near the interface. However, the study by Yang et al. (2020) was limited by its nature to a low Reynolds number. The objective of the current study is to investigate whether their conclusions hold under higher Reynolds number conditions, investigated through experimental data. In the current study, we focus on the experimental analysis of the TNTI in a TBL exposed to an APG at a high friction Reynolds number, $Re_\tau = 7500$. Here, $Re_\tau = \delta_{99}U_\tau/\nu$ where δ_{99} is the boundary layer thickness, U_τ is the friction velocity and ν is the kinematic viscosity of the fluid. The APG flow evolves from canonical ZPG upstream history conditions (interested readers may refer to Deshpande et al. (2023) for a complete definition). The datasets are validated for the ZPG case in terms of streamwise and wall-normal velocity statistics, with comparisons made to the studies of Baidya et al. (2017), Morrill-Winter et al. (2015) and Marusic et al. (2024). Spanwise vorticity is also considered with comparisons to the study of Morrill-Winter et al. (2015) who conducted extensive analyses for ZPG high Re_τ wall-bounded flows. The TNTI is detected using vorticity and local kinetic energy (LKE) methods applied to high-magnification PIV measurements. While vorticity and LKE methods have been prevalent in TNTI research, both cater to distinct data sources and analysis needs, with vorticity methods often aligned with DNS data and LKE methods favoured for experimental data due to their robustness against noise. A concise overview of common methods for detecting the TNTI interface is presented in Table 1, where the main parameters (Z_i, σ_i) are characterised as:

$$\overline{Z_i} = \langle Z_n \rangle, \quad \sigma_i = \sqrt{\langle (Z_n - \overline{Z_i})^2 \rangle}. \tag{1}$$

The key characteristics are illustrated in the schematic shown in Fig. 1, where Z_n represents the mean height for each snapshot, and σ_i denotes the standard deviation across all images.

For the LKE method analysis, a modified LKE equation is proposed to account for APG conditions, as detailed in Section 4.2 (Eq. (8)). Determining the TNTI height requires identifying appropriate TNTI thresholds. Lee et al. (2017) employed joint probability density functions (JPDFs) of wall-normal height and vorticity to delineate the flow regions. They identified an irrotational region in the free stream, a rotational region near the wall, and an intermittent region between them. Their methodology for determining thresholds involves identifying the intersection of the lowest contour slope in the wake region and the centres of mass in the intermittency region from JPDF.

In this study, the same approach is applied using the spanwise vorticity and the modified LKE JPDF to determine TNTI thresholds for both ZPG and APG conditions. Additionally, an investigation is conducted into the complexity and dynamics of the TNTI through conditional averaging of instantaneous velocity profiles (*i.e.*, without removing the mean). Conditional averaging of instantaneous streamwise and wall-normal velocities provides insights into the interface's behaviour under APG conditions in comparison to previously studied ZPG TBLs.

Throughout this paper, flow properties denoted by capital letters and overbars represent absolute parameters averaged in the streamwise direction and time, while those with tildes represent instantaneous values. Lowercase letters represent fluctuations about their respective means. The Cartesian coordinate system (x, y, z) represents the streamwise, spanwise, and wall-normal directions, respectively, with U, V, and W representing the associated velocity components.

2. Experimental details

The experiments were conducted in the High Reynolds Number Boundary Layer Melbourne Wind Tunnel (HRNBLWT, Marusic et al. (2015), Deshpande et al. (2023)) at a streamwise location $x = 17.5$ m. The friction velocity (U_τ) was measured using oil film interferometry (OFI) for both the ZPG and APG conditions (Marusic et al., 2024). A droplet of silicone oil (50 cSt) is applied and spread on the smooth wall surface in the wind tunnel. This droplet is illuminated by a monochromatic light source, which, when the tunnel is operated at the desired speed, creates clear fringes that are captured with a DSLR camera. More details about the wall shear stress measurements are described in Marusic et al. (2024). The total uncertainty using OFI, considering oil viscosity calibration, fringe extraction, and the possibility of dust contamination, is estimated to be within ±1.5%.

2.1. APG setup

The HRNBLWT facility (Marusic et al., 2015; Deshpande et al., 2023) allows precise control of the pressure gradient via air bleeds. The air bleeds are created with spanwise slots in the tunnel ceiling, located every 1.2 m along its 27 m long working section. Fig. 2(a) shows a schematic of the test section with the air bleed locations. To assess the pressure gradient, we computed the pressure coefficient (C_p) as

$$C_p(x) = 1 - \left(\frac{U_\infty}{U_{\infty(x=1)}} \right)^2, \tag{2}$$

where U_∞ is the freestream velocity measured with a Pitot-static tube at each x location. At the start of the working section C_p is maintained constant at $C_p \approx 0$ in the ZPG region up to $x = 8.0$ m by introducing blockage through spanwise slots in the ceiling, see Fig. 2(b). The APG region at $x > 8.0$ m is regulated using meshes at the outlet of the test section. These meshes are made of perforated steel sheets, each with a porosity of 51%. A total of 3 meshes are used to form the current

Nomenclature

English symbols

C_p	Pressure coefficient [–]
d	Wire diameter [μm]
f	Aperture size [mm]
k^*	Modified local kinetic energy [–]
l	Wire length [mm]
$p_{\tilde{\Omega}_y^*,z_i}(\tilde{\Omega}_y^*)/p_{\tilde{k}^*,z_i}(\tilde{k}^*)$	One-dimensional PDF of vorticity/LKE [–]
Re_τ	Friction Reynolds number [–]
T_{zones}	Binary turbulent/non-turbulent matrix [–]
$T_{\text{interface},\tilde{\Omega}_y^*}$	Smoothing of TNTI spanwise vorticity [–]
$T_{\text{interface},\tilde{k}^*}$	Smoothing of TNTI modified LKE [–]
U	Streamwise velocity [m/s]
U_∞	Freestream velocity [m/s]
U_τ	Friction velocity [m/s]
$U\|_i$	Conditionally averaged streamwise velocity [m/s]
u	Streamwise velocity fluctuation [m/s]
W	Wall-normal velocity component [m/s]
$W\|_i$	Conditionally averaged wall-normal velocity [m/s]
w	Wall-normal velocity fluctuation [m/s]
x	Streamwise coordinate [m]
z	Wall-normal coordinate [m]
Z_i	TNTI height [m]
Z_n	TNTI height for each snapshot [m]

Abbreviations

APG	Adverse pressure gradient
FOV	Field of view
HRNBLWT	High Reynolds Number
LKE	Local kinetic energy
OFI	Oil film interferometry
PIV	Particle image velocimetry
TBL	Turbulent boundary layer
TNTI	Turbulent/non-turbulent interface
ZPG	Zero pressure gradient

Greek symbols

β	Clauser pressure gradient parameter [–]
δ_{99}	Boundary layer thickness [m]
δ^*	Boundary layer displacement thickness [m]
$\Gamma_{\tilde{\Omega}_y^*,z}/\Gamma_{\tilde{k}^*,z}$	JPDF of spanwise vorticity/LKE and wall-normal height [–]
ν	Kinematic viscosity [m^2/s]
ν_T	Eddy viscosity [m^2/s]
σ_i	Standard interface height deviation [m]
τ_0	Wall shear stress [N/m^2]
Ω_x	Streamwise vorticity [1/s]
Ω_y	Spanwise vorticity [1/s]
Ω_z	Wall-normal vorticity [1/s]
ω_y	Spanwise vorticity fluctuation [1/s]
$\Omega_{y,th}^+$	Spanwise vorticity threshold [–]

Subscripts/superscripts/operators

$\overline{(\cdot)}$	Time-averaged quantity
$(\cdot)^+$	Quantity normalised by viscous units

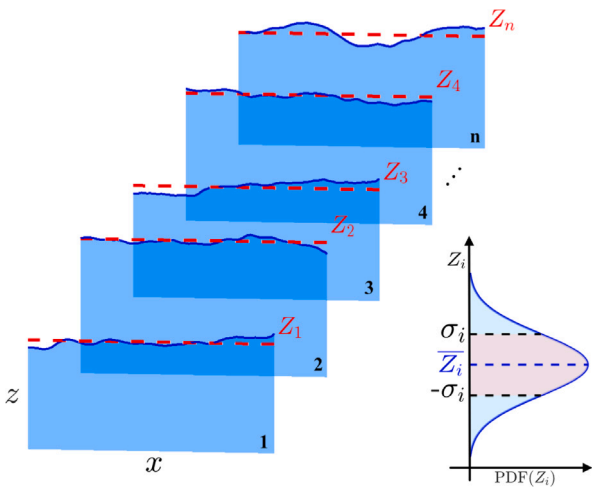

Fig. 1. Schematic representation of TNTI parameters: mean interface height (Z_i) and standard deviation (σ_i) for each snapshot, used to characterise TNTI heights across n snapshots. The red dashed line represents the mean interface height for each snapshot along the streamwise direction. (For interpretation of the references to colour in this figure legend, the reader is referred to the web version of this article.)

APG. Further details of the APG setup can be found in Deshpande et al. (2023).

The freestream turbulence level was also checked for both the ZPG and APG configurations, as this can be an influencing factor for TNTIs. At the measuring station, the freestream turbulence level from hot-wire measurements was 0.3% for ZPG and 0.5% for the APG, which are sufficiently low levels so as to not influence the relevant outer region flow physics (Coles, 1962).

2.2. Particle image velocimetry configuration

To obtain detailed measurements throughout the boundary layer, four high-resolution Imager CX-25 cameras with 12-bit resolution were arranged vertically, as illustrated in Fig. 3(*a*). Each camera was equipped with Tamron SP AF 180 mm macro lenses, set to an aperture size of $f/11$, allowing a digital resolution of 22 μm per pixel. Illumination was provided by an InnoLas SpitLight Compact PIV 400 dual-pulse Nd:YAG laser, using a combination of spherical and cylindrical lenses. A section of the tunnel floor is constructed from glass to facilitate laser passage while minimising reflections in the vicinity of the wall.

Both PIV measurements, conducted for high-Reynolds-number ZPG and APG TBL, were taken at the same streamwise location, $x \approx 17.5$ m (Fig. 2(*a*)). Polyamide tracers, ranging from 1 to 2 μm in diameter, were used to seed the flow. The resulting stitched field-of-view (FOV) was 104×441 mm^2 (in $x \times z$). Laser pulses and camera synchronisation were achieved using a programmable timing unit (PTU X, LaVision GmbH), controlled by DaVis 10.1 software.

A total of 2000 double-frame image pairs were recorded with a laser pulse separation of 50 μs, resulting in a maximum particle displacement of 10 pixels in the freestream region at $U_\infty = 12.6$ m/s. Camera calibration was performed using a 2-D target featuring 1 mm diameter dots, spaced 5 mm apart. To enhance the signal-to-noise ratio, the minimum intensity from the image ensemble was subtracted, followed by normalisation using the average intensity. Multi-pass cross-correlation was applied with a final interrogation window size of 24 × 24 pixels (0.53×0.53 mm^2) and a 50% overlap. These parameters, along with the laser sheet thickness, correspond to viscous-scaled spatial resolutions along $\Delta x^+ \times \Delta y^+ \times \Delta z^+$ to be 18 × 55 × 18 and 11 × 43 × 11 for the ZPG and APG cases, respectively, with the spanwise average corresponding to the thickness of the laser sheet. Here, the superscript '+' denotes normalisation with the friction velocity U_τ and kinematic

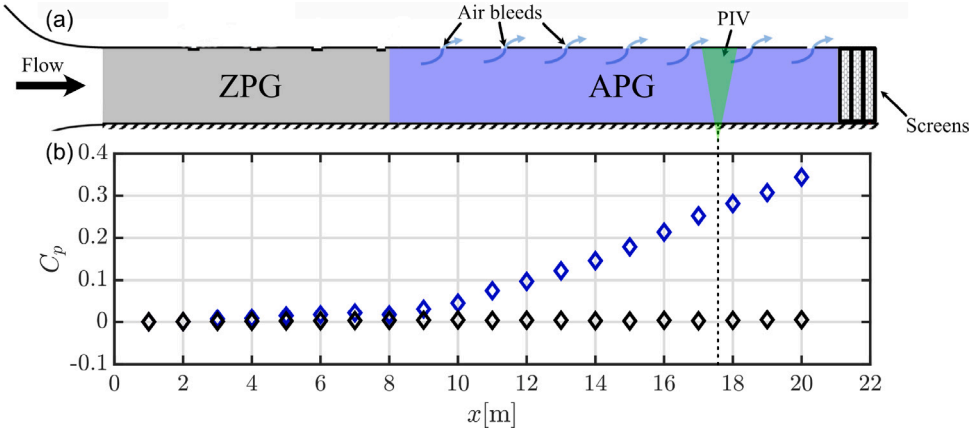

Fig. 2. (*a*) Schematic image of the test section for the APG case, with 3 meshes located at the outlet of the test section. Canonical inflow ZPG until $x \approx 8$ m and the APG section at $x > 8$ m. The green sheet and dashed line indicates the PIV measurement location, located at $x \approx 17.5$ m. (*b*) Distribution of the pressure coefficient (C_p) at certain streamwise locations (x). In (*b*), (◇) and (◇) represent the ZPG and APG cases, respectively. (For interpretation of the references to colour in this figure legend, the reader is referred to the web version of this article.)

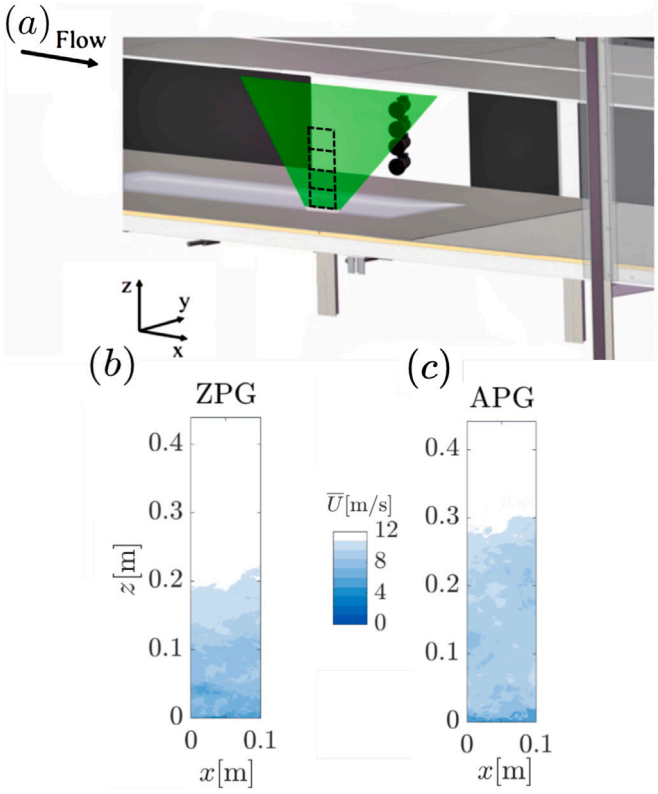

Fig. 3. (*a*) Experimental setup with tower planar PIV cameras arranged in the HRNBLWT. The four black high-resolution cameras at the back of the tunnel create a large FOV, which covers the entire turbulent boundary layer with high and consistent resolution. (*b-c*) The plots of the FOV show instantaneous flow for ZPG (*b*) and APG (*c*) cases.

viscosity ν. Deshpande et al. (2023) have previously shown based on hotwire experiments that this spanwise resolution does not influence the mean statistics in the outer region of high-Re_τ APG TBLs, at least for presently-considered moderate β-ranges ($\lesssim 2$).

A notable aspect of this PIV dataset is its high wall-normal resolution ($\Delta z^+ \sim$ 10–20 across the entire boundary layer), which is of the order of most well-resolved TBL simulations in the outer (*i.e.*, TNTI) region, making it well-suited for capturing and analysing the TNTI. Further details are provided in Table 2. Figs. 3(*b*) and (*c*) show

Table 2
PIV experiment parameters.

Parameters	Unit	ZPG/APG
Digital resolution	[μm/pixel]	22
Field of view	$x \times z$ [mm^2]	105 × 440
PIV sampling window	$x \times z$ [pixel]	24 × 24
	$x \times z$ [mm^2]	528 × 528
	$x^+ \times z^+$	18 × 18/11 × 11
Overlap	%	50
Frequency	Hz	9.5

representative snapshots of the instantaneous streamwise velocity U in the $x \times z$ plane for the ZPG and APG TBLs, respectively. The annotated FOVs for each camera illustrate the effective positioning of the camera setup. In the ZPG case, the boundary layer thickness, estimated by δ_{99}, falls within the FOV of camera 2. For the APG TBL, δ_{99} is located near the centre of camera 3. This arrangement ensures comprehensive, high-resolution velocity measurements of the entire boundary layer in both ZPG and APG experiments.

3. Flow statistics

In this study, two new PIV data sets were acquired and analysed (ZPG and APG cases), and all other data presented in the paper have been previously published and described in Table 3. First, we examine the mean viscous scaled streamwise ($\overline{U}^+$) velocity with Reynolds normal stress ($\overline{u^2}^+$) from the current PIV (ZPG-PIV, APG-PIV) and hot-wire data (ZPG-HW1, APG-HW (Marusic et al., 2024)) at the same friction Reynolds number (Table 3). This data was collected using in-house fabricated single streamwise hot-wire sensors made from Wollaston wires, which were soldered onto a Dantec 55P05 probe. The sensors utilised wires with a diameter of $d = 2.5\,\mu$m, ensuring an aspect ratio of $l/d \gtrsim 200$ to minimise end-conduction effects (Hutchins et al., 2009).

We only consider data beyond $z^+ \approx 30$ to avoid statistics influenced by near-wall laser reflection and poor spatial resolution effects. Figs. 4(*a, b*) display the inner-scaled mean velocity profiles and streamwise variance for the ZPG and APG cases. We observe excellent agreement for the first- and second-order statistics with the hot-wire data. Additionally, we confirmed that for streamwise mean velocity APG case, the wake region started to peel off earlier due to the pressure gradient, and a slight downward shift in the log-region (Deshpande et al., 2023). As expected, the variance results for APG are characterised by a fuller profile in the outer region compared to the ZPG flow (Harun et al., 2013). Although previously published low Re_τ data at similar APG

Table 3
Details of used databases. Friction Reynolds number is defined as $Re_\tau = \frac{\overline{U}_\tau \delta_{99}}{\nu}$; β the Clauser pressure gradient parameter ($\beta = \frac{\delta^*}{\tau_o}\frac{dP}{dx}$) with $\frac{dP}{dx}$ as the pressure gradient in the streamwise direction; δ^* the boundary layer displacement thickness and τ_o the wall shear stress. Here, HW in the case name denotes data acquired through a hot-wire (Marusic et al., 2024; Baidya et al., 2017; Morrill-Winter et al., 2015; Marusic et al., 2024).

Case	Symbol	x [m]	$\overline{U}_\infty(x=0)$ [m/s]	$\overline{U}_\infty(x)$ [m/s]	Re_τ -	$\frac{\nu}{\overline{U}_\tau}$ [μm]	δ_{99} [mm]	$\beta(x)$ -	Reference
ZPG-PIV		17.5	12.6	12.6	7500	36	270	0	Present
ZPG-HW1	,	17.5	12.6	12.6	7500	36	270	0	Marusic et al. (2024)
ZPG-HW2		18.0	14.8	14.8	8170	32	261	0	Baidya et al. (2017)
ZPG-HW3		18.0	15.3	15.3	7894	32	253	0	Morrill-Winter et al. (2015)
APG-PIV		17.5	12.6	11.2	7100	46	328	1.4	Present
APG-HW	,	17.5	12.6	11.2	7100	46	328	1.4	Marusic et al. (2024)

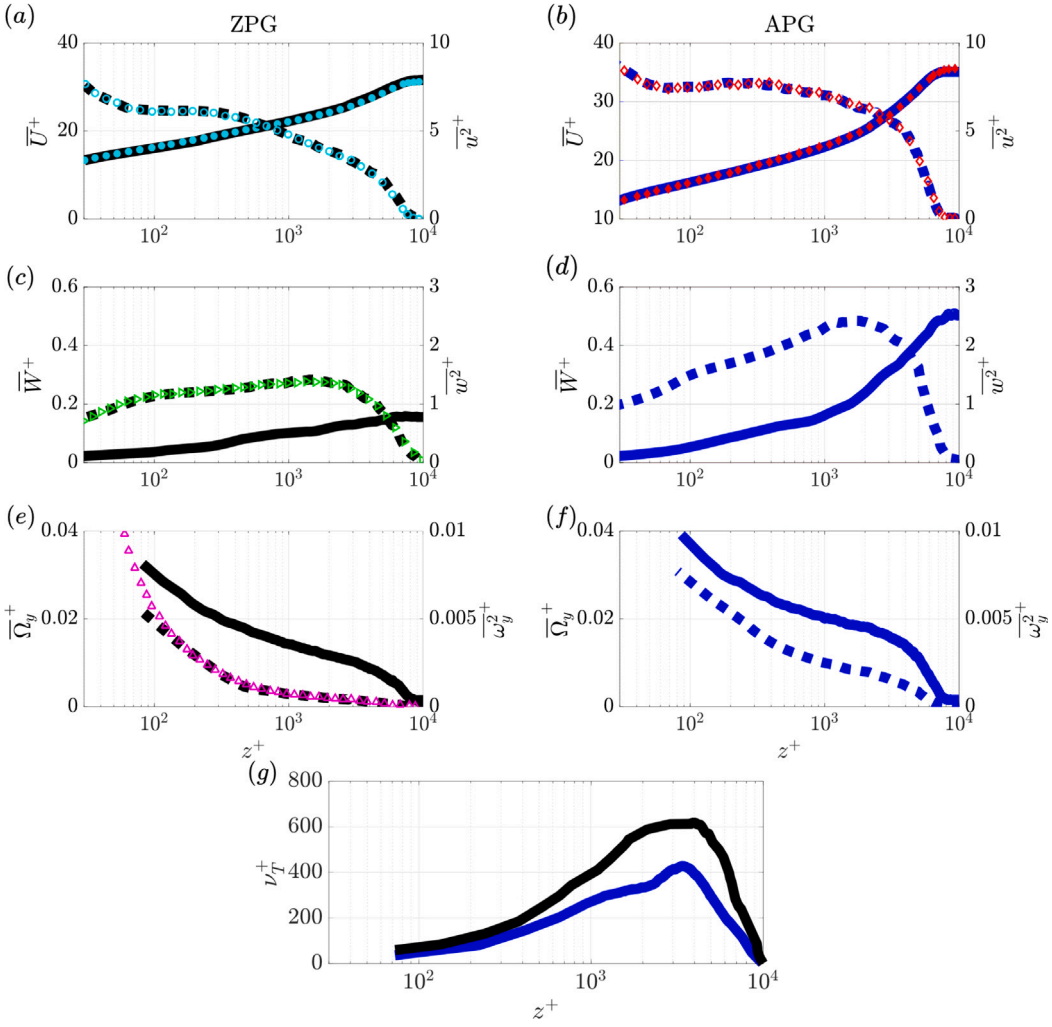

Fig. 4. (*a-d*) Comparison of zero pressure gradient (ZPG) and adverse pressure gradient (APG) mean velocity profiles ($\overline{U}^+$, $\overline{W}^+$) and their corresponding variance profiles ($\overline{u^2}^+$, $\overline{w^2}^+$). (*e-f*) Mean vorticity ($\overline{\Omega_y}^+$) and its fluctuations ($\overline{\omega_y^2}^+$). All mean profiles are plotted with solid lines, while variance profiles are represented by dashed lines. Black and blue lines denote ZPG and APG conditions, respectively. Symbol ● refers to mean ZPG streamwise velocity for case ZPG-HW1, while ○ refers to its variance. Symbol ◆ refers to mean APG streamwise component for case APG-HW, while ◇ refers to its variance. Other symbols for plotted data correspond to Table 3. (*g*) Eddy viscosity ($\nu_T{}^+$). The $^+$ superscript indicates normalisation with viscous units ($U^+ = U/\overline{U}_\tau$, $\omega^+ = \omega \times \nu/\overline{U}_\tau^2$) . (For interpretation of the references to colour in this figure legend, the reader is referred to the web version of this article.)

strengths (β) exhibit a distinct outer peak in the u-variance (Monty et al., 2011; Bobke et al., 2017), the present high Re_τ cases are associated with significantly weaker small-scale energy in the outer region than low Re_τ cases, resulting in the absence of an outer peak (readers are referred to Deshpande et al. (2023) for further details).

The mean wall-normal component ($\overline{W}^+$) and its variation ($\overline{w^2}^+$) are plotted in Figs. 4(*c,d*), where the ZPG case shows strong agreement with the ZPG-HW2 case, which has similar conditions. Baidya et al. (2017) utilised a custom ×-probe with dimensions of 0.4×0.4 mm ($l_x \times l_z$) in the x- and z-directions, and a wire separation of 0.2 mm (Δs_y) in the y-direction. We see that with the pressure gradient, fluctuations in the wall-normal component become more prominent, as expected, as does the mean wall-normal component. Further, the mean spanwise vorticity ($\overline{\Omega}_y^+$),

$$\tilde{\Omega}_y = \frac{\partial \tilde{U}}{\partial z} - \frac{\partial \tilde{W}}{\partial x} \tag{3}$$

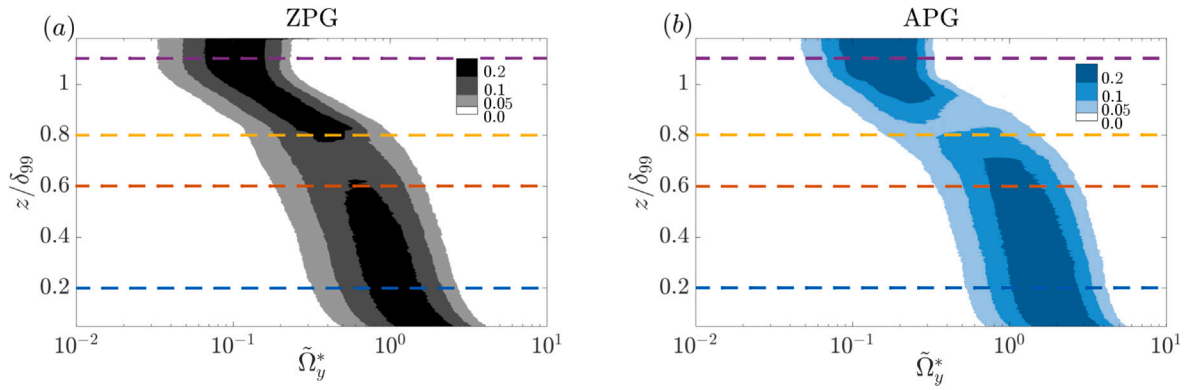

Fig. 5. The spanwise vorticity JPDF, $\Gamma_{\tilde{\Omega}_y^*,z}$, for ZPG (*a*) and APG (*b*) illustrates the joint probability distribution of spanwise vorticity and wall-normal distance. The dashed lines indicate the wall-normal locations ($z/\delta_{99} = [0.2, 0.6, 0.8, 1.1]$), which are plotted in Fig. 6.

and its variance ($\overline{\omega_y^2}^+$) are plotted in Figs. 4(*e,f*), with data (ZPG-HW3) from Morrill-Winter et al. (2015) for the ZPG case in Fig. 4(*e*). Morrill-Winter et al. (2015) conducted an extensive analysis of vorticity using an experimental dataset at a similar Re_τ in the same wind tunnel at the University of Melbourne (Table 3). They used "Mini-Foss" multi-element hot-wire probe for data acquisition which is based on the design of Foss and Haw (1990). The probe includes a vertical ×-array arranged at nominal angles of ±45° relative to the z-direction. This setup captures the instantaneous velocity components $\tilde{u}$ and $\tilde{v}$, indicated by the tilde symbol. Additionally, the ×-array is supplemented by two single wires aligned parallel to the wall and oriented perpendicular to the mean flow direction. The vorticity shown is normalised in viscous units ($\nu/\overline{U_\tau^2}$). We observe excellent agreement for the ZPG case (Fig. 4(*e*)). We note that both the mean spanwise vorticity and its fluctuations increase with the pressure gradient.

For completeness, we also compare the eddy viscosity for the ZPG and APG cases, described as follows:

$$\nu_T^+ = \frac{\overline{-uw}^+}{\left(\frac{\partial \tilde{U}}{\partial z}\right)^+}, \tag{4}$$

which is commonly used in turbulence modelling studies (Stephen et al., 2000). Tsikata and Tachie (2013) conducted an experimental study of fully developed turbulent channel flow and APG turbulent channel flow over smooth and rough walls at low Re_τ using PIV. Their findings showed that the difference in eddy viscosity over rough walls compared to smooth wall data is negligible. Additionally, it was found that eddy viscosity decreases with APG flow in the outer region, as has been observed previously at lower Reynolds numbers. The present data, shown in Fig. 4(*g*), demonstrates that this trend persists at high Reynolds numbers, with significantly lower eddy viscosity observed throughout the boundary layer in the APG case.

4. TNTI detection

4.1. Vorticity

The vorticity method for detecting the TNTI (Bisset et al., 2002; de Silva et al., 2013) is characterised by the magnitude of vorticity, defined as $|\Omega| = \sqrt{\Omega_x^2 + \Omega_y^2 + \Omega_z^2}$, where Ω_x, Ω_y, and Ω_z are the vorticity components in the streamwise, spanwise, and wall-normal directions, respectively. Here, with planar PIV data, we are restricted to the spanwise component of vorticity, denoted as Ω_y (Eq. (3)). Watanabe et al. (2018) demonstrated that a nearly identical TNTI location can be obtained using the spanwise vorticity magnitude $|\omega_y|$ in TBLs compare to the passive scalar method. Also, Bisset et al. (2002) have shown that the spanwise vorticity is dominant component in the TNTI.

Computing partial derivatives from raw PIV data can be challenging, as even minor disturbances can lead to significant noise amplification in the vorticity calculations. Towards addressing this issue, velocity gradients are determined using a second-order least squares method (Eisma et al., 2015) and Gaussian smoothing was applied to the spatial domain with a filter width of $\sigma \approx 10z^+$ to reduce noise in the dataset (Wieneke, 2017; Atkinson et al., 2011; Eisma et al., 2015). This process effectively smoothed the spanwise vorticity magnitude without significantly altering the overall data structure.

To determine the vorticity threshold, a JPDF (Fig. 5) was computed based on the method by Lee and Zaki (2018), which has also been used in the work by Yang et al. (2020). The JPDF, $\Gamma_{\tilde{\Omega}_y^*,z}$, of spanwise vorticity and wall-normal height is computed by binning the values of spanwise vorticity, $\tilde{\Omega}_y^*$, and the corresponding wall-normal positions, z, into a 2D histogram, where each bin count represents the occurrence of a specific combination of $\tilde{\Omega}_y^*$ and z across the dataset. Further details on how the thresholds are determined are provided in Section 4.2 and illustrated in Fig. 7, where the same method is applied to the LKE JPDF.

Using vorticity, the TBLs were categorised into the fully turbulent region ($\tilde{\Omega}_y^* > 10^0$) and the irrotational region ($\tilde{\Omega}_y^* < 10^{-2}$ for ZPG and $\Omega_y^* < 10^{-1}$ for APG). The intermittent region lies between these two regions. Here, the spanwise vorticity is normalised using viscous units, and the friction Reynolds number, $\Omega_y{}^* = |\Omega_y| \left(\frac{\nu}{U_\tau^2}\right) \sqrt{Re_\tau}$, following Borrell and Jiménez (2016) and Lee et al. (2017).

Ideally, we would like to use the same thresholds and diagnostic method used by Yang et al. (2020). However, this is not possible due to the inherent problem caused by the signal-to-noise ratio in the experimental data being much lower than in the DNS (Borrell and Jiménez, 2016; Yang et al., 2020), and thus the small-scale structures/vorticities are not completely resolved.

Borrell and Jiménez (2016) reported a distinct transition from large-scale to small-scale vorticities exhibiting bimodal behaviour in the premultiplied JPDF of wall-normal distance and vorticity magnitude for low Re_τ ZPG DNS data at $z/\delta_{99} = 0.75$. This serves as an initial indication of the resolution quality of the JPDF when comparing the vorticity and LKE methods.

Bimodal behaviour in a PDF plot is characterised by two distinct smaller peaks on either side of the distribution, separated by a plateau in the middle. The first peak corresponds to the irrotational flow region in the outer layer, while the second peak represents the rotational flow region near the wall. The plateau in the middle indicates the intermittent region between these two flow states. To investigate this, Fig. 6 presents the plot of $p_{\tilde{\Omega}_y^*,z_i}(\tilde{\Omega}_y^*)$,

$$p_{\tilde{\Omega}_y^*,z_i}(\tilde{\Omega}_y^*) = \Gamma_{\tilde{\Omega}_y^*,z_i}(\tilde{\Omega}_y^*) \tag{5}$$

representing the one-dimensional marginal distribution of the JPDF for certain height (z_i), $\Gamma_{\tilde{\Omega}_y^*,z_i}$, which was binned over the two variables (vorticity and height).

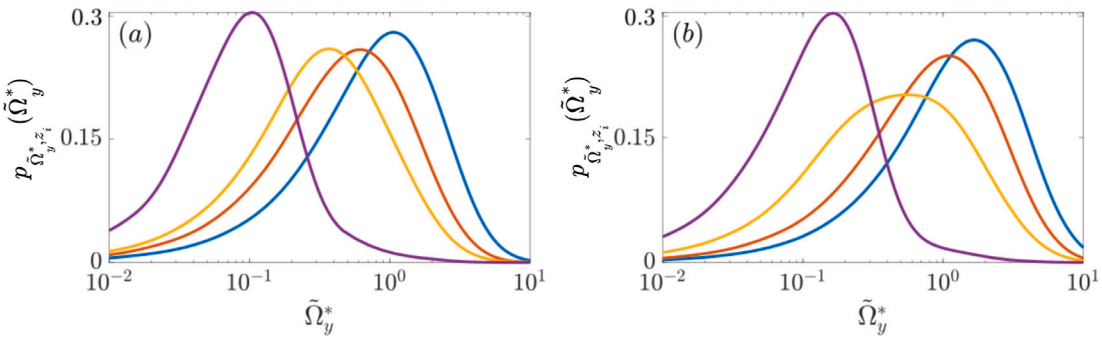

Fig. 6. (*a,b*) show the one-dimensional PDF, $p_{\tilde{\Omega}_y^*,z_i}(\tilde{\Omega}_y^*)$, of spanwise vorticity and wall-normal location for ZPG (*a*) and APG (*b*) at four different wall-normal locations as shown in Fig. 5 with matched colours ($z/\delta_{99} = [0.2, 0.6, 0.8, 1.1]$).

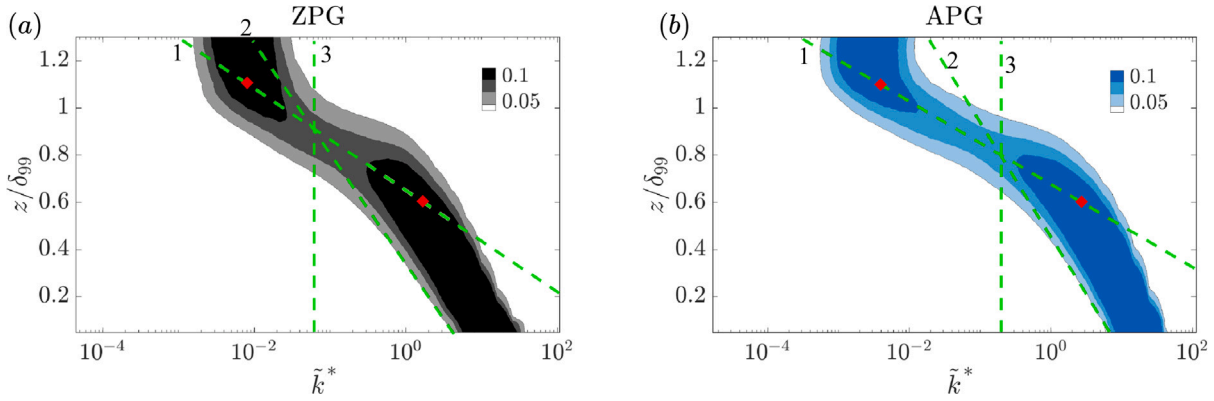

Fig. 7. The JPDF, $\Gamma_{\tilde{k}^*,z}$, for ZPG (*a*) and APG (*b*) depicts the joint probability density function for LKE and wall-normal distance. The green vertical line indicates the LKE threshold (3), which intersects with two green dashed lines. The first line (1) connects the two centres of mass (♦) in the intermittent region, while the second line (2) represents the slope of the lowest contour in the wake region. (For interpretation of the references to colour in this figure legend, the reader is referred to the web version of this article.)

The MATLAB function *smooth*, using a moving average span of 10, is utilised to ensure the smoothed curve closely adheres to the original data's magnitude and shape while effectively eliminating sharp edges. Furthermore, two distinct locations in the intermittent region, $z/\delta_{99} = 1.1$ and $z/\delta_{99} = 0.6$, have been utilised to identify the centres of mass, corresponding to the peaks in the PDF distribution (Fig. 6). This method of plotting the centres of mass in the JPDF figure is employed for threshold determination, which is explained in detail in Section 4.2. Here, the vorticity method does not exhibit clear bimodal peaks for either the ZPG or APG cases. Therefore, this method for detecting TNTI does not perform well for the given PIV dataset.

To find the interface height, a binarization algorithm is first used to determine the turbulent zones as

$$T_{\text{zones}} = \begin{cases} 1, & \text{if } \tilde{\Omega}_y^* > \tilde{\Omega}_{y,th}^* \\ 0, & \text{otherwise.} \end{cases} \tag{6}$$

Additionally, smoothing of the vorticity field is conducted over four neighbouring cells.

$$T_{\text{interface},\tilde{\Omega}_y} = \begin{cases} 1, & \text{if } \sum_{p=i-4}^{i+4} \sum_{q=j-4}^{j+4} T_{\text{zones}(p,q)} = 81 \\ 0, & \text{otherwise.} \end{cases} \tag{7}$$

This adjustment was necessary to eliminate noise in the data and to enhance the visibility of the interface, making it easier to model. The variables p and q represent the indices used to iterate along the streamwise and wall-normal directions, respectively, within the 2D matrix. These indices allow for the evaluation of each cell's neighbourhood in the matrix during the interface detection process.

In summary, due to the lack of bimodal behaviour and the poorly resolved JPDF for the reasons mentioned, we conclude that using vorticity for the current experiments is not the best approach. Hence, we subsequently focus on the LKE method.

4.2. Local kinetic energy

Despite the vorticity method being the preferred method for TNTI detection (Bisset et al., 2002; Jiménez et al., 2010), in our experimental study we need to adopt another method. One of the most prominent alternative methods for PIV studies in air is to use the local kinetic energy (LKE). Watanabe et al. (2018) and Chauhan et al. (2014) utilised the LKE method in their analysis of DNS and experimental data, respectively. Watanabe et al. (2018) demonstrated that the intermittency factor obtained using the LKE method shows good agreement between turbulent regions identified by the LKE and those based on vorticity magnitude.

Using the LKE method for APG flows requires a modification to the approach presented by Chauhan et al. (2014), which was prescribed for ZPG flows. In APG flows, the wall-normal velocity ($\overline{W}_\infty$) can be non-zero and significant and thus needs to be included in the analysis. Therefore, we use the general form of local kinetic energy equation

$$\tilde{k}^* = 100 \times \frac{1}{9U_\infty^2} \sum_{m,n=-1}^{1} \left[\left(\tilde{U}_{m,n} - \overline{U}_\infty \right)^2 + \left(\tilde{W}_{m,n} - \overline{W}_\infty \right)^2 \right]. \tag{8}$$

To determine the threshold, the same JPDF method used for vorticity is employed, as explained in . Here, this method by Lee et al. (2017) is applied to LKE JPDF, $\Gamma_{\tilde{k}^*,z}$, and results are shown in Fig. 7. Intersection of the slope of the lowest contour in the wake region (green dashed line "2") and the line which connects two centres of mass in the intermittent region (green dashed line "1") is chosen as threshold. The centres of mass are indicated with ♦ in the intermittent region for $z/\delta_{99} = 1.1$ and $z/\delta_{99} = 0.6$. The PDF distributions for these slices are also presented in Fig. 8(*a,b*), where the centre of mass corresponds to the peak in their PDF distribution. This intermittent section is between low local kinetic energy ($\tilde{k}^* < 10^{-2}$) and full turbulent region ($\tilde{k}^* >$

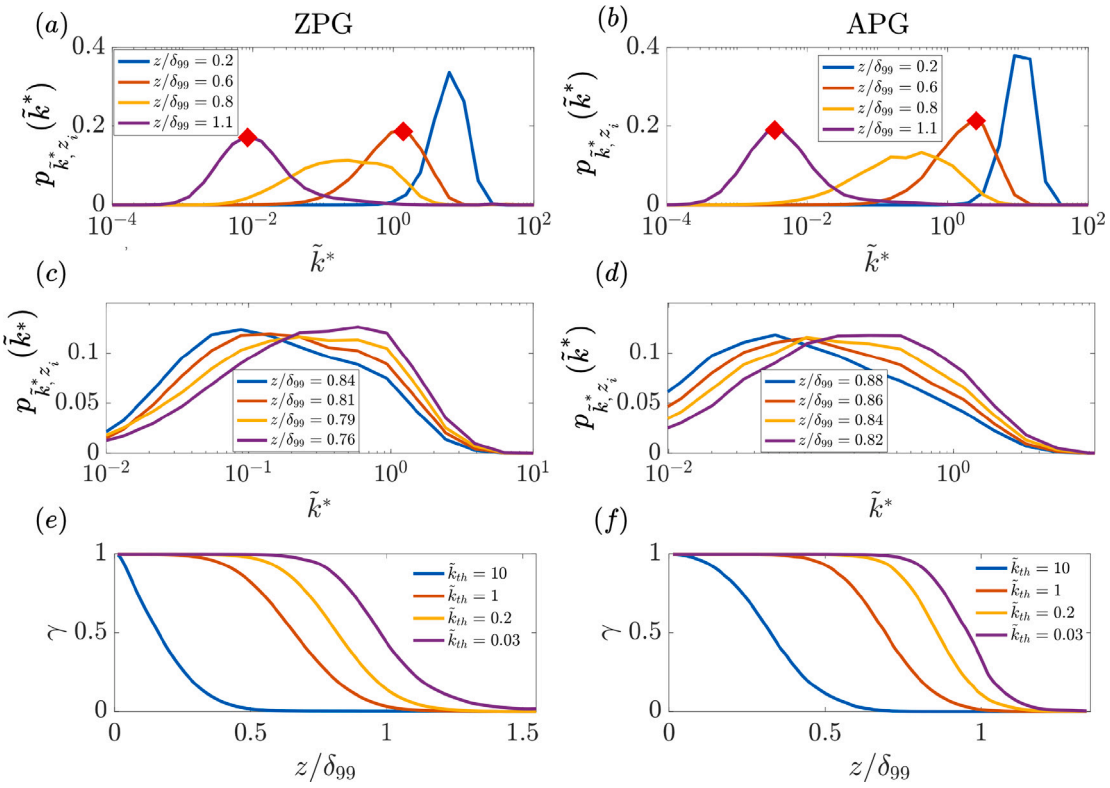

Fig. 8. (*a,b*) show the one-dimensional PDF, $p_{\tilde{k}^*,z_i}(\tilde{k}^*)$, of LKE and wall-normal location for ZPG (*a*) and APG (*b*) for the four different wall-normal locations (z/δ_{99}) from Fig. 7, while (*c,d*) show one-dimensional PDF, $p_{\tilde{k}^*,z_i}(\tilde{k}^*)$, for more wall-normal locations around bimodal behaviour. (*e,f*) Illustrates the intermittency factor (γ) for various LKE thresholds ($\tilde{k}^*_{th}$).

10^0). The slope of the lowest contour in the wake region is steeper for the APG case, whereas the slope connecting the two centres of mass in the intermittent region is lower for the APG case compared to the ZPG case.

The thresholds for $\tilde{k}^*$ based on the two intersection lines (Fig. 7) are $\tilde{k}^*_{th} = 0.06$ and $\tilde{k}^*_{th} = 0.2$ for ZPG and APG, respectively. In order to determine the TNTI height, the turbulent zones are identified using

$$T_{\text{zones}} = \begin{cases} 1, & \text{if } \ln(\tilde{k}^*) > \ln(\tilde{k}^*_{th}) \\ 0, & \text{otherwise} \end{cases} \tag{9}$$

and, subsequently, the smoothing of the vorticity field is calculated using

$$T_{\text{interface},k^*} = \begin{cases} 1, \text{ if } \sum_{p=i-2}^{i+2} \sum_{q=j-2}^{j+2} T_{\text{zones}(p,q)} = 25 \\ 0, \text{ otherwise.} \end{cases} \tag{10}$$

In this context, the same notations as in Eq. (7) are used. However, due to higher noise and less resolved vorticity caused by the computation of velocity gradients, the use of four neighbouring cells was initially considered. However, using two neighbouring cells has been found to be sufficient for the local kinetic energy method, as it provides better resolution of the data and reduces noise.

Fig. 8 shows various features of the LKE JPDF. Fig. 8 (*a,b*) shows the one-dimensional PDF, $p_{\tilde{k}^*,z_i}(\tilde{k}^*)$

$$p_{\tilde{k}^*,z_i}(\tilde{k}^*) = \Gamma_{\tilde{k}^*,z_i}(\tilde{k}^*) \tag{11}$$

for horizontal slices of $\Gamma_{\tilde{k}^*,z}$ at the same wall-normal distances as in Fig. 6 (*a,b*) for the vorticity. We now observe a trend with a clearer plateau, which is closer to quasi-bimodal behaviour compared to the vorticity method. This is especially evident in Figs. 8(*c,d*), where more locations around the plateau region are plotted. The tendency remains the same, with less distributed areas close to the wall and in the free stream, while $z/\delta_{99} = 0.8$ exhibits a lower peak and wider distribution. The most significant difference is observed close to the wall, with higher PDF peaks for APG. Finally, the intermittency factor, defined as

$$\gamma(z;\tilde{k}^*_{th}) = \int_{\tilde{k}^*_{th}}^{\infty} \Gamma_{\tilde{k}^*,z}\, \mathrm{d}\tilde{k}^* \Big/ \int_0^{\infty} \Gamma_{\tilde{k}^*,z}\, \mathrm{d}\tilde{k}^* \tag{12}$$

is computed based on different thresholds and is shown in Figs. 8(*e,f*). This represents the turbulent probability at various wall-normal heights, as determined by Eq. (9), where a value of 1 indicates turbulence and 0 indicates non-turbulence. While there is almost no change for the low and mild $\tilde{k}^*_{th}$ between ZPG and APG, for the high threshold ($\tilde{k}^*_{th} = 10$), we observe a larger drop for the ZPG case close to the wall, which confirms that APG is more robust to higher thresholds.

4.3. Interface height statistics

A primary measure of the TNTI is its mean interface height, $\overline{Z}_i$. For this, the instantaneous TNTI height, $z_i(x)$, was first determined using the algorithms described above, using Eq. (10) for LKE and Eq. (7) for vorticity, and adopting the thresholds obtained from the JPDF as described in the previous section. The mean value for each PIV flow field, Z_i, was then found by averaging across the streamwise domain for each image (see Fig. 1). Fig. 9 shows the normalised normal distribution for computed mean height (Z_i/δ_{99}) and standard deviation (σ_i/δ_{99}), obtained across the 2000 images; the black-coloured lines are for ZPG and the blue-coloured lines are for APG. As was found by Yang et al. (2020) at lower Reynolds numbers, the mean normalised TNTI height decreases with adverse pressure gradient.

However, it is also noted that the two methods (LKE and vorticity) give very similar mean TNTI heights (as documented in Table 1), and this is despite the LKE method being more suitable for the current experimental data, having displayed a clearer bimodal behaviour between the inner and outer regions in the JPDF compared to the vorticity method.

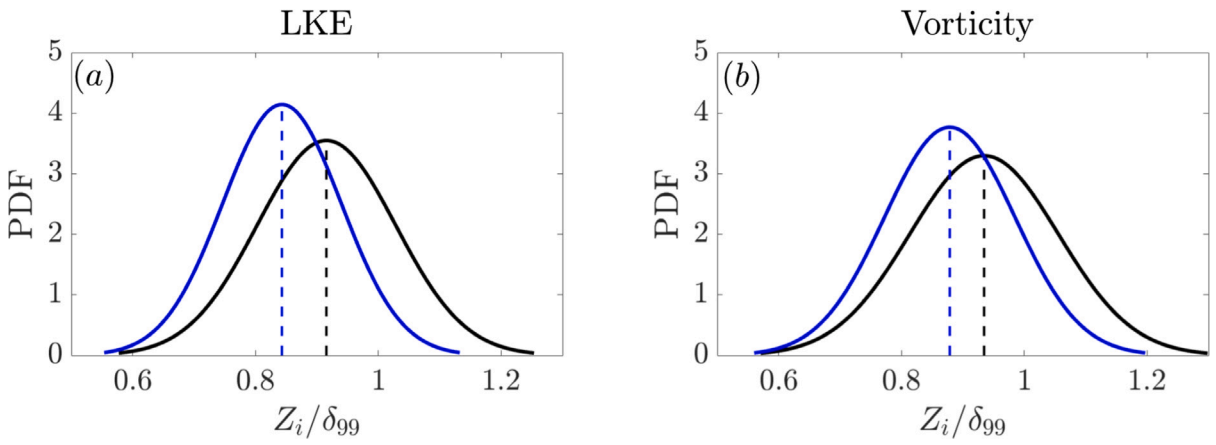

Fig. 9. The probability density functions for selected TNTI heights for ZPG (black) and APG (blue). (a) Using the LKE method, with thresholds $\tilde{k}^*_{th} = 0.06$ for ZPG and $\tilde{k}^*_{th} = 0.2$ for APG. (b) Using the vorticity method, with thresholds $\tilde{\Omega}^*_{y,th} = 0.13$ for ZPG and $\tilde{\Omega}^*_{y,th} = 0.305$ for APG. (For interpretation of the references to colour in this figure legend, the reader is referred to the web version of this article.)

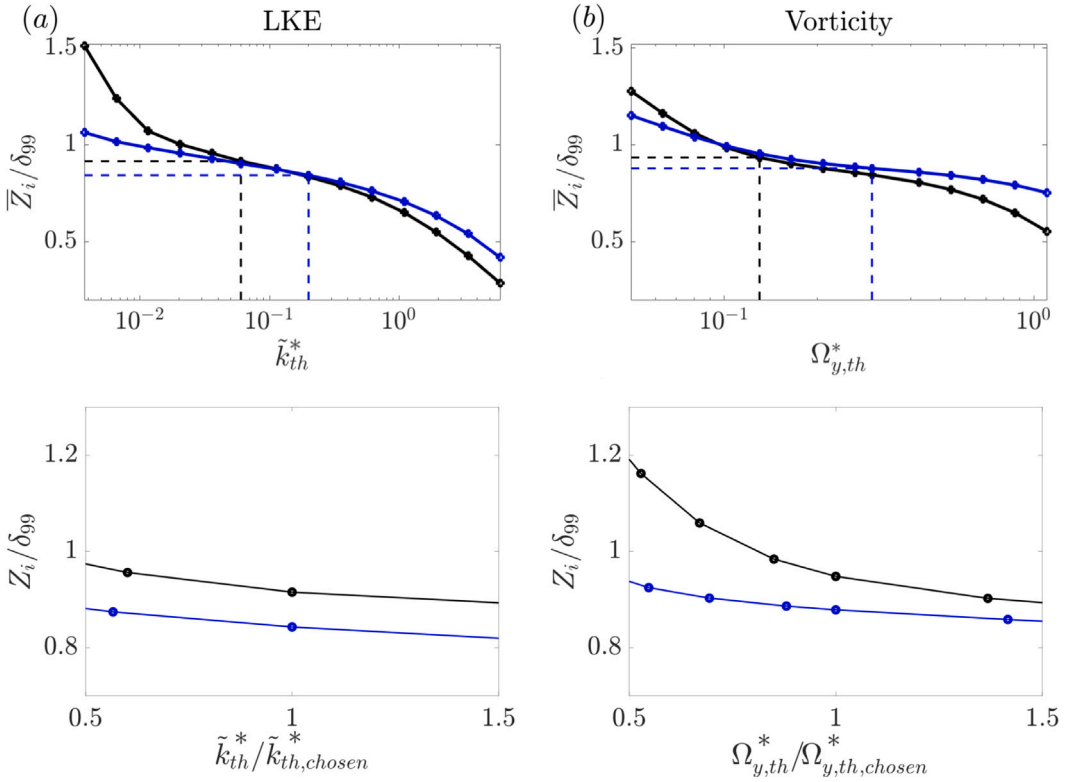

Fig. 10. (*a,b*) Mean interface heights ($\overline{Z_i}/\delta_{99}$) for varying thresholds. The vertical dashed lines indicate the chosen thresholds. (*c,d*) Sensitivity of the mean interface height to the chosen threshold for ± 50% variation to the chosen threshold. ZPG (black), APG (blue). (For interpretation of the references to colour in this figure legend, the reader is referred to the web version of this article.)

In order to assess the robustness of the quantitative results of the TNTI height statistics, it is important to consider the sensitivity to the threshold level for both the LKE and vorticity methods. Figs. 10(*a,b*) shows how different threshold levels affect the estimates for the average TNTI height, $\overline{Z_i}$, normalised by the boundary layer thickness. The range of thresholds were chosen based on the minimum and maximum values for the LKE and vorticity methods. For both the LKE and vorticity methods, we observe similar trends, with the APG cases showing less sensitivity to the chosen threshold level. When $\tilde{k}^* < \tilde{k}^*_{th}$ and $\Omega^*_y < \Omega^*_{y,th}$, the mean normalised TNTI height is seen to be higher for ZPG, while when $\tilde{k}^* > \tilde{k}^*_{th}$ and $\Omega^*_y > \Omega^*_{y,th}$, the mean normalised TNTI height is lower for ZPG compared to APG. To more directly compare LKE threshold sensitivity to that of vorticity, Figs. 10(*c,d*) show the respective thresholds normalised to the JPDF determined thresholds for each case. The results show that a ±50% change in threshold level leads to the mean normalised TNTI height changing by 10% for ZPG and 7% for APG for the LKE method. In the case of the vorticity method, this variation increases to 33% for ZPG and 10% for APG. The very high sensitivity for the vorticity method affirms the problematic nature of this method, as noted from the lack of bimodal behaviour for the JPDF. While the LKE method is clearly more suitable than the vorticity

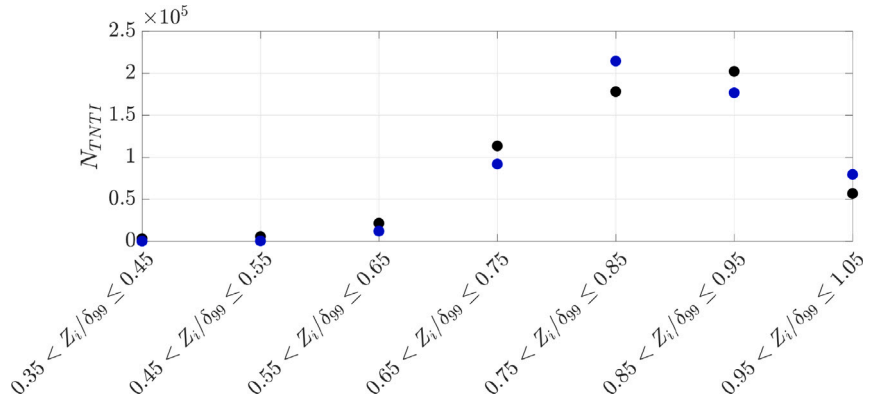

Fig. 11. N_{TNTI} represents the count of interface heights within a specified domain for ZPG (•) and APG (•).

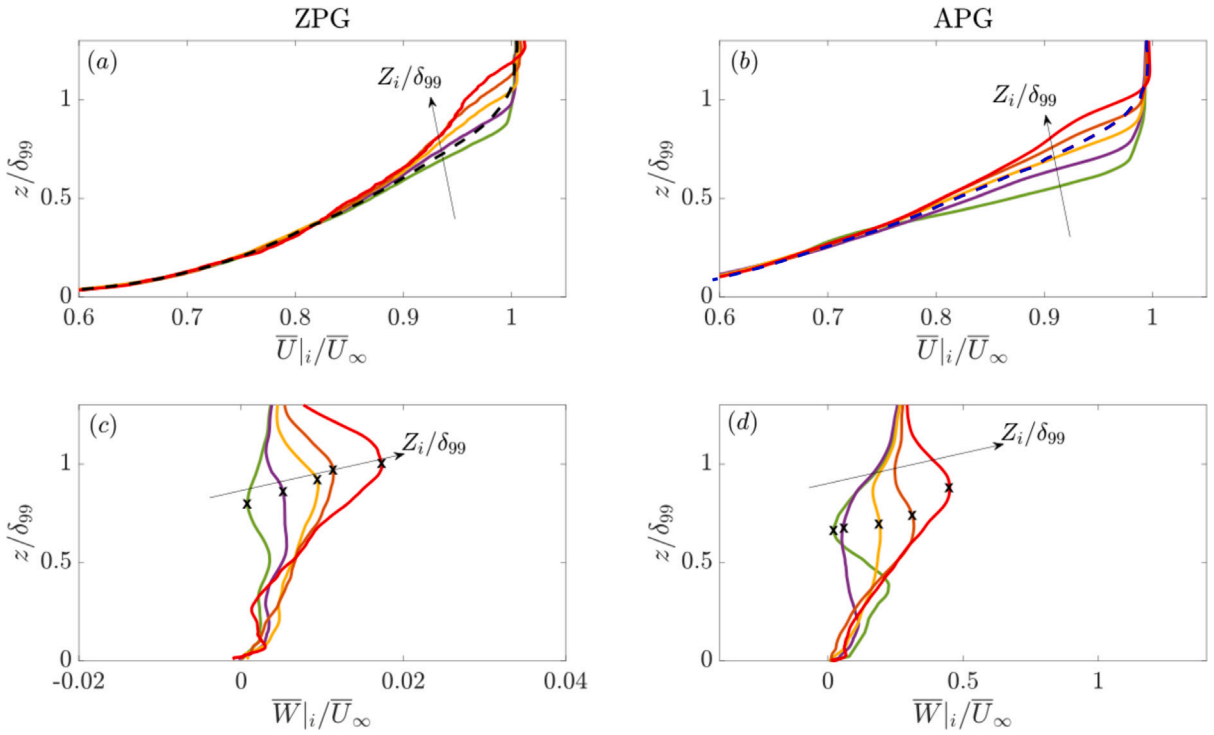

Fig. 12. Conditional averaged profiles of streamwise (a,b)), $U|_i$, and wall-normal (c,d), $W|_i$, velocity for different TNTI height (Z_i/δ). (——) is average profile when $0.95 < Z_i/\delta_{99} \leq 1.05$;(——) profiles are for $0.85 < Z_i/\delta_{99} \leq 0.95$ and so on up to $0.55 < Z_i/\delta_{99} \leq 0.65$(——). Mean U/U_∞ is shown in (a) and (b) as dashed black and blue lines, respectively. × indicates the bulk wall-normal velocity for each bin.. (For interpretation of the references to colour in this figure legend, the reader is referred to the web version of this article.)

method for these experiments, LKE still has a relatively high level of sensitivity to the adopted threshold level.

5. Conditional analysis

In this section, we analyse the conditionally averaged profiles of streamwise velocity ($U|_i$) and wall-normal velocity ($W|_i$) for various bands or domains of TNTI height (Z_i/δ), using the LKE method. Here "$|_i$" indicates averaging in seven different domains. This analysis seeks to provide information on the observed decrease in normalised TNTI height with the imposition of APG, and to understand how the differences in mean U and W profiles between ZPG and APG in the wake region (Fig. 4) are associated with different domains of TNTI location.

Seven different domains are considered: $0.35 < Z_i/\delta_{99} \leq 0.45$ to $0.95 < Z_i/\delta_{99} \leq 1.05$. Fig. 11 shows the total number for each domain. The APG case is likely unresolved in both $U|_i$ and $W|_i$ for smaller TNTI domains, as fewer TNTI heights are found in these regions. Furthermore, we observe that in the APG case, $U|_i$ exhibits the highest concentration of TNTI heights between 0.75 and 0.85, whereas in the ZPG case, this concentration occurs between 0.85 and 0.95.

Fig. 12 shows the conditionally averaged instantaneous streamwise (a,b) and wall-normal (c,d) velocities for the ZPG and APG cases. For the ZPG case, the conditional profiles begin to deviate at $Z_i/\delta_{99} \approx 0.85$, while for the APG cases, the deviation occurs considerably closer to the wall at $Z_i/\delta_{99} \approx 0.75$.

Fig. 12(a) for the ZPG case also confirms sharp transitions in wall-normal gradients near the TNTI region, as previously documented by Chauhan et al. (2014) and others. The mean velocity profile (– –) is seen to most closely follow the conditionally averaged profile $0.65 < Z_i/\delta_{99} \leq 0.75$. The APG case (Fig. 12($b$)), in comparison, shows a mean velocity profile lifted closer to the domain $0.75 < Z_i/\delta_{99} \leq 0.85$, and the gradient close to the boundary layer edge is less prominent compared to the ZPG case. Additionally, it is observed that for the APG case, the spread in the conditional averaged curves is larger than in the

ZPG case, which is consistent with the start of the deviation from the mean velocity profile occurring closer to the normalised position from the wall.

For the wall-normal velocity, Fig. 12(*c*) shows a predominantly positive bulk $\overline{W}|_i/\overline{U}_\infty$ for the highest Z_i/δ_{99} domain above $z/\delta_{99} \approx 0.65$ for the ZPG case, consistent with Chauhan et al. (2014). This indicates an upward velocity related to the TNTI being lifted away from its mean height location. Conversely, the lowest Z_i/δ_{99} domain shows a predominantly lower bulk $W|_i$ throughout the outer part of the boundary layer, aligning with the observations by Chauhan et al. (2014) that the TNTI is pushed towards the wall. Under the APG scenario (Fig. 12(*d*)), interesting similarities and differences compared to the ZPG case are observed. Notably, a more prominent change in $\overline{W}|_i/\overline{U}_\infty$ is evident. While higher Z_i/δ_{99} domains exhibit a similar trend to the ZPG case with a positive bulk $\overline{W}|_i/\overline{U}_\infty$ in the TNTI region, smaller Z_i/δ_{99} domains show a predominantly higher bulk $\overline{W}|_i/\overline{U}_\infty$. The locations of the peak $\overline{W}|_i/\overline{U}_\infty$, however, are observed to occur closer to the wall in the APG case (marked as × in Fig. 12 (*c,d*)) and with a more pronounced intensity. These features are consistent with a more dynamic TNTI, acting across the boundary layer, in the APG case leading to a lower $\overline{Z_i}/\delta_{99}$ compared to the ZPG case.

6. Conclusions

The implementation of a high-magnification tower PIV system with four cameras in the Melbourne HRNBLWT enabled a detailed investigation of turbulent boundary layers under APG and ZPG conditions, with a particular focus on the TNTI. Both LKE and vorticity methods were employed to detect the TNTI. The high spatial resolution achieved by this setup allowed for precise measurements of TNTI characteristics across ZPG and APG conditions at high friction Reynolds numbers.

The analysis began with a validation of first- and second-order ensemble-averaged statistics for streamwise and wall-normal velocities and spanwise vorticity under ZPG conditions, providing a robust basis for comparison with APG cases. APG effects were shown to significantly amplify these statistical quantities in the outer regions of the flow, indicating more pronounced turbulence levels and structural changes in the boundary layer as the pressure gradient increased.

JPDFs for LKE/vorticity and wall-normal distance were used to determine TNTI thresholds and associated mean heights, facilitating a comparison of TNTI characteristics across pressure gradient conditions. Although both methods revealed consistent trends across thresholds, limitations in the PIV data became evident. The vorticity method was found to be less reliable due to its sensitivity to in-plane velocity components, which can lead to inaccuracies in detecting TNTI boundaries. The LKE method, on the other hand, exhibiting a characteristic bimodal behaviour in the JPDF, proved more effective in delineating turbulent and non-turbulent regions. A sensitivity analysis further confirmed the limitations of using spanwise vorticity and emphasised the relative reliability of the LKE method for this experimental configuration, while acknowledging that the LKE method also has inherent constraints due to its dependency on in-plane measurements. Additionally, we have shown that a ±50% change in the threshold level results in the mean normalised TNTI height changing by approximately 4–5 times more for the vorticity method compared to the LKE method. The very high sensitivity of the vorticity method highlights its problematic nature, as noted by the lack of bimodal behaviour in the JPDF. However, based on both methods, we observe that for the chosen threshold, the normalised TNTI height decreases with APG.

Further, conditional averaging of the streamwise velocity reveals greater dispersion in the outer region for the APG case. Notably, a more significant change in $W|_i/U_\infty$ is observed, where the bulk positive $W|_i/U_\infty$ is more prominent across the entire conditionally averaged profile for the APG case.

The implications of these findings extend to improved modelling of boundary layer flows in adverse pressure gradient environments, particularly in high Reynolds number applications where TNTI behaviours can critically impact mixing and energy transport. The study also underscores the limitations of current TNTI detection methods for 2D PIV data, advocating for the need to further refine and validate techniques such as the LKE approach under varying flow conditions and in three-dimensional setups.

In conclusion, the present study provides an analysis of TNTI characteristics under adverse pressure gradients, revealing insights into boundary layer dynamics at high Reynolds numbers. Future work should explore three-dimensional PIV and alternative TNTI detection methods to more accurately capture the complex, turbulence interactions induced by pressure gradients in turbulent boundary layer flows.

CRediT authorship contribution statement

Luka Lindić: Writing – original draft, Validation, Methodology, Investigation, Formal analysis, Data curation, Conceptualization. **Wagih Abu Rowin:** Writing – review & editing, Data curation. **Rahul Deshpande:** Writing – review & editing, Supervision, Conceptualization. **Ivan Marusic:** Writing – review & editing, Supervision, Funding acquisition, Conceptualization.

Declaration of competing interest

The authors declare that they have no known competing financial interests or personal relationships that could have appeared to influence the work reported in this paper.

Acknowledgments

The authors are grateful to Drs. Tom Jelly and Massimiliano Nardini for helpful comments and feedback on the manuscript, and Dr. Mitchell Lozier for providing the freestream turbulence data. The financial support of the Office of Naval Research (ONR) is gratefully acknowledged with funding from ONR global grant: N62909-23-1-2068. R. D. is grateful for financial support from the University of Melbourne's Postdoctoral Fellowship.

Data availability

Data will be made available on request.

References

Atkinson, C., Coudert, S., Foucaut, J.M., Stanislas, M., Soria, J., 2011. The accuracy of tomographic particle image velocimetry for measurements of a turbulent boundary layer. Exp. Fluids 50, 1031–1056.

Baidya, R., Philip, J., Hutchins, N., Monty, J., Marusic, I., 2017. Distance-from-the-wall scaling of turbulent motions in wall-bounded flows. Phys. Fluids 29 (2).

Bisset, D.K., Hunt, J.C., Rogers, M.M., 2002. The turbulent/non-turbulent interface bounding a far wake. J. Fluid Mech. 451, 383–410.

Bobke, A., Vinuesa, R., Örlü, R., Schlatter, P., 2017. History effects and near equilibrium in adverse-pressure-gradient turbulent boundary layers. J. Fluid Mech. 820, 667–692.

Borrell, G., Jiménez, J., 2016. Properties of the turbulent/non-turbulent interface in boundary layers. J. Fluid Mech. 801, 554–596.

Chauhan, K., Philip, J., De Silva, C.M., Hutchins, N., Marusic, I., 2014. The turbulent/non-turbulent interface and entrainment in a boundary layer. J. Fluid Mech. 742, 119–151.

Chen, C.H.P., Blackwelder, R.F., 1978. Large-scale motion in a turbulent boundary layer: a study using temperature contamination. J. Fluid Mech. 89 (1), 1–31.

Coles, D., 1962. The turbulent boundary layer in a compressible fluid. Appendix A: A manual of experimental boundary-layer practice for low-speed flow. Technical Report R-403-PR, USAF The Rand Corporation.

Corrsin, S., Kistler, A.L., 1955. Free-stream boundaries of turbulent flows. NASA.

de Silva, C.M., Philip, J., Chauhan, K., Meneveau, C., Marusic, I., 2013. Multiscale geometry and scaling of the turbulent-nonturbulent interface in high Reynolds number boundary layers. Phys. Rev. Lett. 111 (4), 044501.

Deshpande, R., Van Den Bogaard, A., Vinuesa, R., Lindić, L., Marusic, I., 2023. Reynolds-number effects on the outer region of adverse-pressure-gradient turbulent boundary layers. Phys. Rev. Fluids 8 (12), 124604.

Eisma, J., Westerweel, J., Ooms, G., Elsinga, G.E., 2015. Interfaces and internal layers in a turbulent boundary layer. Phys. Fluids 27 (5).

Foss, J., Haw, R., 1990. Transverse vorticity measurements using a compact array of four sensors. Heuris. Therm. Anemom. 97, 71–76.

Harun, Z., Monty, J.P., Mathis, R., Marusic, I., 2013. Pressure gradient effects on the large-scale structure of turbulent boundary layers. J. Fluid Mech. 715, 477–498.

Hedley, T.B., Keffer, J.F., 1974. Turbulent/non-turbulent decisions in an intermittent flow. J. Fluid Mech. 64 (4), 625–644.

Hutchins, N., Nickels, T.B., Marusic, I., Chong, M., 2009. Hot-wire spatial resolution issues in wall-bounded turbulence. J. Fluid Mech. 635, 103–136.

Jiménez, J., Hoyas, S., Simens, M.P., Mizuno, Y., 2010. Turbulent boundary layers and channels at moderate Reynolds numbers. J. Fluid Mech. 657, 335–360.

Klebanoff, P.S., 1955. Characteristics of turbulence in boundary layer with zero pressure gradient. NASA.

Kovasznay, L.S., Kibens, V., Blackwelder, R.F., 1970. Large-scale motion in the intermittent region of a turbulent boundary layer. J. Fluid Mech. 41 (2), 283–325.

Lee, J., Sung, H.J., Zaki, T.A., 2017. Signature of large-scale motions on turbulent/non-turbulent interface in boundary layers. J. Fluid Mech. 819, 165–187.

Lee, J., Zaki, T.A., 2018. Detection algorithm for turbulent interfaces and large-scale structures in intermittent flows. Comput. & Fluids 175, 142–158.

Marusic, I., Abu Rowin, W., Lozier, M., Lindić, L., Zarei, A., Deshpande, R., 2024. Turbulent/non-turbulent interface in high Reynolds number pressure gradient boundary layers. In: IUTAM Symposium on Turbulent/Non-Turbulent Interface in Turbulent Shear Flows. Springer, http://dx.doi.org/10.48550/arXiv.2412.10645.

Marusic, I., Chauhan, K.A., Kulandaivelu, V., Hutchins, N., 2015. Evolution of zero-pressure-gradient boundary layers from different tripping conditions. J. Fluid Mech. 783, 379–411. http://dx.doi.org/10.1017/jfm.2015.501.

Monty, J.P., Harun, Z., Marusic, I., 2011. A parametric study of adverse pressure gradient turbulent boundary layers. Int. J. Heat Fluid Flow 32 (3), 575–585. http://dx.doi.org/10.1016/j.ijheatfluidflow.2011.02.006.

Morrill-Winter, C., Klewicki, J., Baidya, R., Marusic, I., 2015. Temporally optimized spanwise vorticity sensor measurements in turbulent boundary layers. Exp. Fluids 56 (12), 216.

Murlis, J., Tsai, H., Bradshaw, P., 1982. The structure of turbulent boundary layers at low Reynolds numbers. J. Fluid Mech. 122, 13–56.

Neuhaus, L., Wächter, M., Peinke, J., 2023. The fractal turbulent/non-turbulent interface in the atmosphere. Wind. Energy Sci. Discuss. 2023, 1–19.

Reuther, N., Kähler, C.J., 2018. Evaluation of large-scale turbulent/non-turbulent interface detection methods for wall-bounded flows. Exp. Fluids 59, 1–17.

Semin, N., Golub, V., Elsinga, G., Westerweel, J., 2011. Laminar superlayer in a turbulent boundary layer. Tech. Phys. Lett. 37, 1154–1157.

da Silva, C.B., Hunt, J.C., Eames, I., Westerweel, J., 2014. Interfacial layers between regions of different turbulence intensity. Annu. Rev. Fluid Mech. 46 (1), 567–590.

Sreenivasan, K., Ramshankar, R., Meneveau, C., 1989. Mixing, entrainment and fractal dimensions of surfaces in turbulent flows. Proc. R. Soc. A 421 (1860), 79–108.

Stephen, B.P., et al., 2000. Turbulent flows. Cambridge University Press, pp. 387–457.

Tsikata, J., Tachie, M., 2013. Adverse pressure gradient turbulent flows over rough walls. Int. J. Heat Fluid Flow 39, 127–145.

Škvorc, P., Kozmar, H., 2021. Wind energy harnessing on tall buildings in urban environments. Renew. Sustain. Energy Rev. 152, 111662.

Wang, J., Marusic, I., 2024. Proceedings of the IUTAM Symposium on Turbulent/Non-Turbulent Interface in Turbulent Shear Flows. Springer Nature.

Watanabe, T., Zhang, X., Nagata, K., 2018. Turbulent/non-turbulent interfaces detected in DNS of incompressible turbulent boundary layers. Phys. Fluids 30 (3).

Wieneke, B., 2017. PIV anisotropic denoising using uncertainty quantification. Exp. Fluids 58 (8), 94.

Yang, J., Yoon, M., Sung, H.J., 2020. The turbulent/non-turbulent interface in an adverse pressure gradient turbulent boundary layer. Int. J. Heat Fluid Flow 86, 108704.